Rakenteiden Mekaniikka (Journal of Structural Mechanics)
Vol. 58, No. 1, 2025, pp. 1–15
http://rakenteidenmekaniikka.journal.fi
https://doi.org/10.23998/rm.148803

VERTAISARVIOITU
KOLLEGIALT GRANSKAD
PEER-REVIEWED
www.tsv.fi/tunnus

A 2D mesoscale model for concrete fracture under dynamic loading

Timo Saksala[1], Sulata Dhakal and Reijo Kouhia

Summary In this paper, we present a 2D mesomechanical model for describing concrete fracture behavior under dynamic loading. The aggregate-mortar mesostructure of concrete is explicitly described, while the interfacial transition zone is represented as a weak zone of finite elements around the aggregates. Concrete failure is described by a damage-viscoplasticity model based on the Drucker–Prager yield criterion and the Rankine criterion as the tensile cut-off. For the viscoplastic part of the model, the consistency approach is adopted. In the damage model, separate scalar damage variables are applied for tensile and compressive stress regimes. Uniaxial compression and tension tests are simulated as the numerical examples. The model holds some promise because it reproduces the experimental failure modes in tension and compression, and in dynamic Brazilian disc test, and predicts a realistic compressive-to-tensile strength ratio as well as the strain-rate sensitivity effect for concrete.

Key words: mesoscale, concrete fracture, finite element method, damage-viscoplasticity

Received: 16 October 2025. Accepted: 14 January 2025. Published online: 12 March 2025.

Introduction

Concrete, as the most important construction material, has attracted substantial amount of both experimental (see e.g. [1–4]) and numerical research (see e.g. [5–7]). At the numerical front, concrete research is advanced at three scales [8]: (1) Macroscale with homogenized properties; (2) Mesoscale at which the bi-phasic nature, i.e. the aggregate-mortar as well as the interfacial transition zone (ITZ) between them, is explicitly described; (3) Microscale with sand particles and cement paste. Due to computational limitations, macroscale considerations are necessary at the structural level, e.g. a concrete dam. Microscale studies are also important when considering, e.g. the effect of water-to-cement ratio on concrete mechanical properties [9]. Since the pioneering work by Roelfstra et al. [10], the mesoscales studies have become increasingly popular, as exemplified by [7–14] (note particularly the review papers by Zhang et al. [7] and Thilakarathna et al. [8]).

[1]Corresponding author: timo.saksala@tuni.fi

Mesomechanical modelling of concrete is crucial to correctly predict its fracture behavior. e.g. at the laboratory sample level. Mesoscale model studies provide valuable information on the effect of concrete mix on the macro-properties and the nonlinear behaviour. Moreover, the aggregates induce various fracture toughening effects, such as crack stopping, redirection and branching [15], which cannot be predicted with homogenized models. For these reasons, the mesomechanical modelling is also adopted in the present paper.

There are basically two approaches to model cracks in computational mechanics, i.e. the continuum approach, with the finite element method (FEM) as the foremost representative, and discontinuum or particle approach, based on distinct elements or interacting particles. The latter is naturally more suitable to describe fracture and fragmentation of brittle materials [15]. However, particle methods are computationally intensive due to the required particle and contact tracking and searching procedures (particle neighbors are not fixed like in the continuum methods). Therefore, continuum approach based on the FEM and a damage-viscoplasticity model is chosen in the present study to describe concrete failure, which it can do only in the smeared sense when special enrichment techniques, such as the extended FEM or the embedded discontinuity FEM [9], are not used. This is not such a drawback because networks of adjacent fully damaged finite elements can describe crack-like behavior of concrete in a satisfactory manner when the deformations are small, and the mesh is dense (enough).

Concrete is also a highly strain-rate sensitive material, which manifests as an increase in strength upon increasing loading rate accompanied with a transition from single crack-to-multiple fragmentation [3,4]. The present approach incorporates the strain-rate sensitivity through viscoplasticity.

The rest of this paper is structured as follows. First, the theory of the damage-viscoplasticity model for concrete failure is briefly presented. Then, the method to generate concrete mesostructure is outlined, and, after that, the method is applied in numerical examples. More specifically, numerical uniaxial tension and compression tests are performed on the concrete samples. Finally, the dynamic Brazilian disc test is simulated.

Damage-viscoplasticity model for concrete

The material model for concrete, applied to both cement and aggregates, consists of the linear elastic part up to elastic limits in compression and tension after which softening stage due to failure follows. In the present model, the concrete material is isotropic but heterogeneous due to its bi-phasic nature. Moreover, the model is formulated within the small deformation framework, enabling the additive split of strain tensor into elastic and viscoplastic parts by $\boldsymbol{\varepsilon} = \boldsymbol{\varepsilon}_{\mathrm{e}} + \boldsymbol{\varepsilon}_{\mathrm{vp}}$.

The stress states leading to viscoplastic flow and damage are indicated by the Drucker–Prager (DP) criterion with the Modified Rankine (MR) criterion as a tensile cut-off. Because the strength and stiffness degradation are taken to be governed by the damage model, perfectly viscoplastic behavior is assumed. The bi-surface yield criterion can then be written, along with rate dependent cohesion c and tensile strength σ_{t}, as

$$f_{\mathrm{DP}}(\boldsymbol{\sigma},\dot{\lambda}_{\mathrm{DP}}) = \sqrt{J_2} + \alpha_{\mathrm{DP}} I_1 - k_{\mathrm{DP}} c(\dot{\lambda}_{\mathrm{DP}}), \tag{1}$$

$$f_{\mathrm{MR}}(\boldsymbol{\sigma},\dot{\lambda}_{\mathrm{MR}}) = \sqrt{\sum_{i=1}^{3} \langle \sigma_i \rangle^2} - \sigma_{\mathrm{t}}(\dot{\lambda}_{\mathrm{MR}}), \tag{2}$$

$$c(\dot{\lambda}_{\mathrm{DP}}) = c_0 + s_{\mathrm{DP}} \dot{\lambda}_{\mathrm{DP}},\ \sigma_{\mathrm{t}}(\dot{\lambda}_{\mathrm{MR}}) = \sigma_{\mathrm{t0}} + s_{\mathrm{MR}} \dot{\lambda}_{\mathrm{MR}}, \tag{3}$$

$$\dot{\lambda}_i \geq 0,\quad f_i \leq 0,\quad \dot{\lambda}_i f_i = 0. \qquad (i = \mathrm{DP}, \mathrm{MR}) \tag{4}$$

The symbol meanings here are as follows: I_1 and J_2 are, respectively, the first and the second invariants of the stress tensor $\boldsymbol{\sigma}$ and its deviator ($\boldsymbol{\sigma} - \frac{1}{3}\mathrm{tr}(\boldsymbol{\sigma})$); c_0 and σ_{t0} are the intact cohesion and tensile strength, respectively; $\dot{\lambda}_{\mathrm{DP}}, \dot{\lambda}_{\mathrm{MR}}$ are the rates of the viscoplastic increments; $s_{\mathrm{DP}}, s_{\mathrm{MR}}$ are constant viscosity moduli; σ_i is the ith principal stress with the positive parts obtained through Macauley brackets in the MR criterion (2). The DP parameters, α_{DP} and k_{DP} are expressed in terms of the friction angle φ to match the uniaxial compressive strength: $\alpha_{\mathrm{DP}} = 2\sin\varphi/(3-\sin\varphi)$ and $k_{\mathrm{DP}} = 6\cos\varphi/(3-\sin\varphi)$. It is also worth to note that a more general definition is possible for rates of internal variables, i.e., instead of $\dot{\lambda}_{\mathrm{DP}}$ (similarly for $\dot{\lambda}_{\mathrm{MR}}$), one could use $\dot{\kappa}_{\mathrm{DP}} = \dot{\lambda}_{\mathrm{DP}} k(\boldsymbol{\sigma}, \boldsymbol{\chi})$, where k is a function of stress and some variables $\boldsymbol{\chi}$. In the present case, $k \equiv 1$, and thus $\dot{\kappa}_{\mathrm{DP}} \equiv \dot{\lambda}_{\mathrm{DP}}$. Finally, Equations (4) specify the consistency conditions in the spirit of Wang et al. [16].

The damage part has separate damage variables in tension and compression stress regimes by

$$\omega_{\mathrm{t}}(\varepsilon_{\mathrm{eqvt}}^{\mathrm{vp}}) = A_{\mathrm{t}}\left(1 - \exp\left(-\beta_{\mathrm{t}} \varepsilon_{\mathrm{eqvt}}^{\mathrm{vp}}\right)\right),\ \omega_{\mathrm{c}}(\varepsilon_{\mathrm{eqvc}}^{\mathrm{vp}}) = A_{\mathrm{c}}\left(1 - \exp\left(-\beta_{\mathrm{c}} \varepsilon_{\mathrm{eqvc}}^{\mathrm{vp}}\right)\right), \tag{5}$$

$$\dot{\varepsilon}_{\mathrm{eqvt}}^{\mathrm{vp}} = \tfrac{1}{3}\langle \mathrm{tr}(\dot{\boldsymbol{\varepsilon}}_{\mathrm{vp}}) \rangle,\quad \dot{\varepsilon}_{\mathrm{eqvc}}^{\mathrm{vp}} = \sqrt{\frac{2}{3}\dot{\mathbf{e}}_{\mathrm{vp}} : \dot{\mathbf{e}}_{\mathrm{vp}}}\ ,\ \dot{\mathbf{e}}_{\mathrm{vp}} = \dot{\boldsymbol{\varepsilon}}_{\mathrm{vp}} - \tfrac{1}{3}\mathrm{tr}(\dot{\boldsymbol{\varepsilon}}_{\mathrm{vp}}), \tag{6}$$

$$\dot{\boldsymbol{\varepsilon}}^{\mathrm{vp}} = \dot{\lambda}_{\mathrm{DP}} \frac{\partial g_{\mathrm{DP}}}{\partial \boldsymbol{\sigma}} + \dot{\lambda}_{\mathrm{MR}} \frac{\partial f_{\mathrm{MR}}}{\partial \boldsymbol{\sigma}}, \qquad \text{with } \beta_{\mathrm{t}} = \sigma_{\mathrm{t0}} h_e / G_{\mathrm{Ic}}, \beta_c = \sigma_{\mathrm{c0}} h_e / G_{\mathrm{IIc}}. \tag{7}$$

Here $g_{\mathrm{DP}}(\boldsymbol{\sigma}, \dot{\lambda}_{\mathrm{DP}}) = \sqrt{J_2} + \beta_{\mathrm{DP}} I_1 - k_{\mathrm{DP}} c(\dot{\lambda}_{\mathrm{DP}})$ is the viscoplastic potential, with β_{DP} being similar to α_{DP} but defined with the dilation angle ψ instead of friction angle. In addition, Equations (5) define the tension and compression damage variables, with parameters $A_{\mathrm{c}}, A_{\mathrm{t}}$ controlling the final values of the damage variables, i.e. the lower the values of these parameters, the higher the residual stress. Parameters $\beta_{\mathrm{c}}, \beta_{\mathrm{t}}$ control the ductility of the post peak response. These latter ones are defined by the mode I and II fracture energies G_{Ic} and G_{IIc}. Moreover, $\sigma_{\mathrm{c0}} = 2c_0 \cos(\varphi)/(1 - \sin(\varphi))$ is the compressive strength. Furthermore, h_e is the characteristic length of a finite element, i.e. the softening scheme is element size insensitive. It is emphasized that no separate damage loading functions are needed in this model because the damage is driven by viscoplastic strain only. Thereby, the strain rate sensitivity of the viscoplasticity part naturally carries over to the damage part as well.

The final component of the model specifies how damage variables operate on the stress tensor, i.e., the nominal-effective stress relation. The Lee & Fenves scheme [17] for the nominal-effective stress relation is chosen here:

$$\boldsymbol{\sigma} = (1 - s_{\mathrm{c}}\omega_{\mathrm{t}})(1 - s_{\mathrm{t}}\omega_{\mathrm{c}})\bar{\boldsymbol{\sigma}},\ \bar{\boldsymbol{\sigma}} = \mathbf{C}_e : (\boldsymbol{\varepsilon} - \boldsymbol{\varepsilon}_{\mathrm{vp}}), \tag{8}$$

$$s_{\mathrm{t}} = 1 - w_{\mathrm{t}} r(\bar{\sigma}_i),\ s_{\mathrm{c}} = 1 - w_{\mathrm{c}}(1 - r(\bar{\sigma}_i)),\ 0 \leq w_{\mathrm{t}}, w_{\mathrm{c}} \leq 1, \tag{9}$$

$$r(\bar{\sigma}_i) = \sum_{i=1}^{3}\langle\bar{\sigma}_i\rangle / \sum_{i=1}^{3}|\bar{\sigma}_i|, \tag{10}$$

with $\mathbf{C}_e$ being the elastic stiffness tensor. The stiffness recovery scheme (8) and (9) accounts for the unilateral effects of damage (microcracks). Therein, the notations are as follows: s_t and s_c are stiffness recovery functions depending on the principal nominal stresses, $\bar{\sigma}_i$; Parameters w_t and w_c control the degree of recovery.

The damage and viscoplasticity parts of the model are combined in the effective stress space allowing to separate the corresponding computations so that the stress return mapping is first performed in the effective principal stress space. Then, the damage variables are updated and, finally, the nominal stress is calculated [18]. The computational procedure for these steps is as follows. For a given element strain $\boldsymbol{\varepsilon}^e_{t+\Delta t} = \mathbf{B}^e \boldsymbol{u}^e_{t+\Delta t}$, do:

1. Predict the trial elastic state:

   $\bar{\boldsymbol{\sigma}}_\mathrm{trial} = \mathbf{C}_e : \left(\boldsymbol{\varepsilon}_{t+\Delta t} - \boldsymbol{\varepsilon}_t^\mathrm{vp}\right) \rightarrow \bar{\boldsymbol{\sigma}}^\mathrm{pr}_\mathrm{trial} = \left[\bar{\sigma}_1^\mathrm{trial}\ \bar{\sigma}_2^\mathrm{trial}\ \bar{\sigma}_3^\mathrm{trial}\right]$
   $f_\mathrm{DP}^\mathrm{trial} = f_\mathrm{DP}\left(\bar{\boldsymbol{\sigma}}^\mathrm{pr}_\mathrm{trial}, \dot{\lambda}^t_\mathrm{DP}\right),\ f_\mathrm{MR}^\mathrm{trial} = f_\mathrm{MR}\left(\bar{\boldsymbol{\sigma}}^\mathrm{pr}_\mathrm{trial}, \dot{\lambda}^t_\mathrm{MR}\right)$
2. Check if the failure criteria are violated: If $\max(f_\mathrm{DP}^\mathrm{trial}, f_\mathrm{MR}^\mathrm{trial}) > 0$ then

   Perform *Viscoplastic correction* $\rightarrow \bar{\boldsymbol{\sigma}}^{t+\Delta t},\ \boldsymbol{\varepsilon}^\mathrm{vp}_{t+\Delta t}$
   Else *elastic state correct* $\rightarrow$ EXIT
3. Update the damage variables:

   $\omega_\mathrm{t}^{t+\Delta t} = g_\mathrm{t}\left(\varepsilon_\mathrm{eqvt}^{\mathrm{vp},t+\Delta t}\right), \quad \omega_\mathrm{c}^{t+\Delta t} = g_\mathrm{c}\left(\varepsilon_\mathrm{eqvc}^{\mathrm{vp},t+\Delta t}\right)$
4. Calculate the nominal stress:

   $\boldsymbol{\sigma}^{t+\Delta t} = (1 - s_\mathrm{c}\omega_\mathrm{t}^{t+\Delta t})(1 - s_\mathrm{t}\omega_\mathrm{c}^{t+\Delta t})\bar{\boldsymbol{\sigma}}^{t+\Delta t}$

In this algorithm, $\bar{\sigma}_i^\mathrm{trial}$ is the *i*th principal stress, while g_t and g_c are the damage functions defined in Equation (5).

Solution of global equations of motion

As the present model is applied in transient dynamic applications involving contact/impact, the global finite element discretized equations of motion are solved explicitly in time. Applying the modified Euler method as the time integrator, the solution is proceeded in time as:

$$\mathbf{M}\ddot{\mathbf{u}}_t + \mathbf{f}_t^\mathrm{int}(\mathbf{u}_t, \dot{\mathbf{u}}_t, \omega_\mathrm{t}, \omega_\mathrm{c}) = \mathbf{f}_t^\mathrm{ext} \rightarrow \ddot{\mathbf{u}}_t, \tag{11}$$
$$\dot{\mathbf{u}}_{t+\Delta t} = \dot{\mathbf{u}}_t + \Delta t\ddot{\mathbf{u}}_t, \tag{12}$$
$$\mathbf{u}_{t+\Delta t} = \mathbf{u}_t + \Delta t\dot{\mathbf{u}}_{t+\Delta t}, \tag{13}$$
$$\mathbf{f}_t^\mathrm{int} = \mathbf{A}_{e=1}^{\mathrm{N_{el}}}\int_{\Omega^\mathrm{e}}\mathbf{B}_\mathrm{u}^{\mathrm{e,T}}\boldsymbol{\sigma}(\mathbf{u}_t, \dot{\mathbf{u}}_t, \omega_\mathrm{t}, \omega_\mathrm{c})\mathrm{d}\Omega, \tag{14}$$

where $\mathbf{M}$ is the lumped mass matrix, $\mathbf{f}_t^\mathrm{int}$ is the internal force vector, $\mathbf{B}_\mathrm{u}^\mathrm{e}$ is the kinematic matrix, $\mathbf{A}$ is the standard finite element assembly operator, $\mathbf{f}_t^\mathrm{ext}$ is the external force vector, Δt is the time step, and $\mathbf{u}_t, \dot{\mathbf{u}}_t, \ddot{\mathbf{u}}_t$ are the displacement, velocity and acceleration vector, respectively.

Numerical concrete sample generation

There are many sophisticated methods to generate realistic aggregate-mortar mesostructures of concrete [7,8]. In the present study, we developed a Matlab based code to generate 2D concrete mesostructures and to mesh them with linear triangle elements. The present method is based on the open-source Matlab-codes by Al-Rumaithi [19] and Matlab PDE Toolbox built-in functions, as shown in Figure 1.

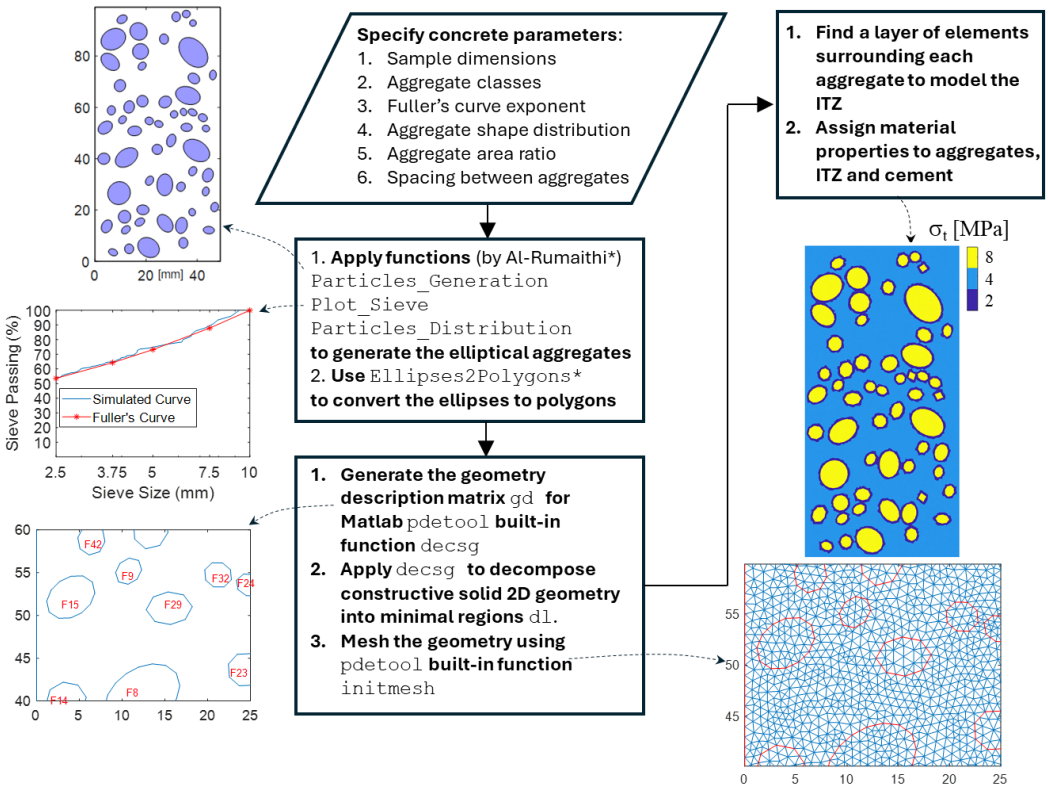

Figure 1. Flowchart of the numerical concrete sample generation (* see [19]).

The method requires the special function `Ellipses2Polygons` because the Matlab built-in function `descg`, to decompose the constructive solid geometry description `gd` into minimal regions `dl`, fails to do it for ellipses but not for polygons. Figure 1 also illustrates the tensile strength distribution of each phase, when the strength of the ITZ is 50 % from that of the mortar. This method has the limitation that the aggregates cannot intersect the sample edges. So, it can model only cast concrete samples, not a cut or machined (out of a larger piece of concrete) ones, at this stage of developments. Finally, the sample shape options are circle and rectangle.

Numerical examples

Material and model parameters

The material properties and model parameters used in the simulations are given in Table 1. The mortar values are averages of the ranges given in www.engineeringtoolbox.com for Portland cement. Moreover, the aggregate values are valid for generic granite gravel.

Table 1. Material properties and model parameter values used in simulations.

Property/Parameter	Mortar Value	Aggregates Value	ITZ Value	Unit
E (Young's modulus)	27.5	60	27.5	GPa
ν (Poisson's ratio)	0.2	0.17	0.2	
ρ (Material density)	2400	2400	2400	kg/m^3
σ_t (Tensile strength)	5	11	2.5	MPa
G_{Ic} (Mode I fracture energy)	0.02	0.04	0.02	N/m
G_{IIc} (Mode II fracture energy)	0.2	0.04	0.2	N/m
c_0 (Cohesion)	9	25	9	MPa
s_{MR} (Viscosity in tension)	0.005	0.005	0.005	MPa·s/m
s_{DP} (Viscosity in compression)	0.005	0.005	0.005	MPa·s/m
A_t (Final value of damage)	0.98	0.98	0.98	
A_c (Final value of damage)	0.98	0.98	0.98	
ϕ (Internal friction angle)	30	50	50	°
ψ (Dilation angle)	5	5	5	°

The values for viscosity moduli given in Table 1 are low test values that have negligible effect at very low strain rates. The effect of these moduli is that the higher their values, the higher the stresses at certain strain rates. Their values are to be adjusted by uniaxial tension and compression tests at the target strain rate.

Uniaxial tension and compression tests

The performance of the present method is now demonstrated in uniaxial tension and compression tests on numerical concrete. These are the crucial tests any predictive modelling code should be able to reproduce both in terms of the correct compressive to tensile strength ratio and macrofailure modes. The numerical concrete samples, i.e. their aggregate-mortar mesostructures, as well as an example of the finite element mesh are shown in Figure 2.

Figure 3 shows the theoretical Fuller's curve and the simulated curves for the numerical samples. This curve represents a grading of aggregate particles resulting in optimum density and strength of the concrete mixture [20]. All the samples in Figure 2 are generated with the same parameters, which are as follows: Aggregate class diameters [1 3/4 1/2 3/8 1/4]×10 mm; Fuller's curve exponent $\alpha = 0.45$; Aggregate shape distribution factor $m = 3$ (see [19,20]); Aggregate area ratio $f_{agg} = 0.6$; Spacing factor between aggregates $er = 0.1$. Despite the same parameter values, each sample generated with the method differs in terms of the aggregate location and their orientation due to their randomness in the code.

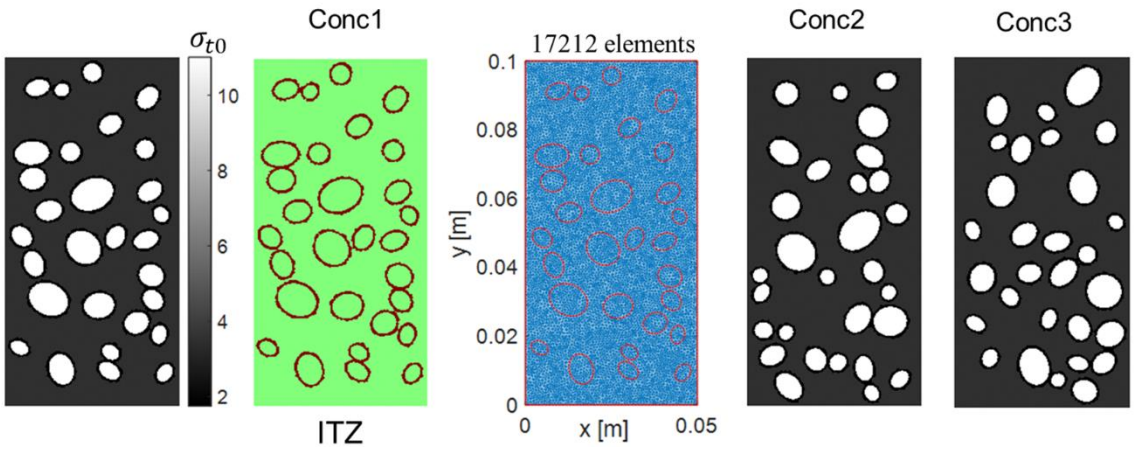

Figure 2. Numerical concrete samples: Aggregate-mortar mesostructure represented in terms of tensile strength distribution, an example of the ITZ and the finite element mesh (consisting of 17212 linear triangle elements) for Conc1.

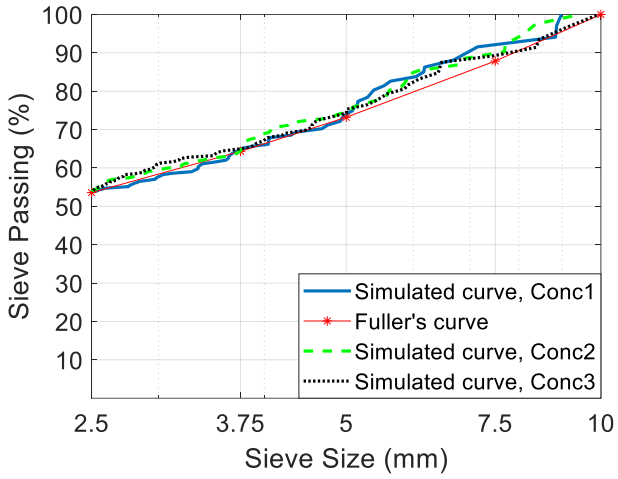

Figure 3. Theoretical and simulated Fuller's curve for numerical concrete samples.

The uniaxial tests are carried out by imposing constant boundary velocity at the upper edge of the sample, while the bottom edge is simply supported. A constant velocity of 0.025 m/s, resulting in a strain rate of 0.25 s^{-1}, is applied. The simulation results for the tensile test are shown in Figure 4. In each case, the predicted failure mode has two cracks initiating at the vertical edges of the sample and propagating horizontally towards the opposite edge. The vertical distance of the cracks varies so that the cracks coalesce only with Conc3. The predicted failure mode is the experimental transverse splitting with the double crack system. The corresponding stress-strain curves, which do not deviate much, show a tensile strength of ~2.5 MPa for each sample. The stiffness determined from the first, linear part of the response is approximately 32 GPa.

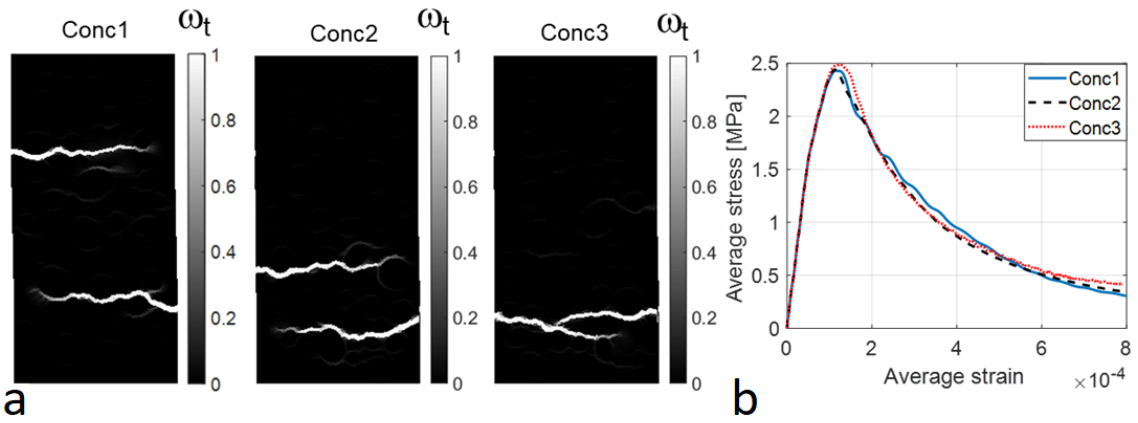

Figure 4. Simulation results for uniaxial tension test: (a) Failure modes in terms of tensile damage distributions; (b) Corresponding average stress-strain curves.

A notable feature in the stress-strain response is the pre-peak nonlinearity, which is not due to the constitutive model for the concrete because it is linear up to the tensile strength for each phase. The pre-peak nonlinearity is due to the heterogeneity of the mesostructure: the weak ITZ areas, surrounding each aggregate, start to fail first, which leads to the observed nonlinear pre-peak response. It can be argued that this is what happens in the experiments, i.e. microcracking events occur at weak spots all over the sample volume, and it is the degraded stiffness induced by microcracking that is reflected in the stress-strain curve, representing the sample net behavior, as nonlinear pre-peak response. It should also be stressed that it is misleading to call such pre-peak response "hardening", when it has nothing to do with the real hardening phenomenon found in metals.

Next, the uniaxial compression test is carried out to the concrete samples. The results are shown in Figure 5. The failure modes predicted with samples Conc1 and Conc2 exhibit typical shear band with single crack for Conc2 and double crack system for Conc1. The corresponding stress-strain responses in Figure 5b, show mild pre-peak nonlinear part and then, after reaching the compressive strength of 26 MPa at the peak, drop abruptly. In drastic contrast, while the stress-strain responses are nearly identical for Conc1 and Conc2, Conc3 attests a compressive strength reaching almost 90 MPa. The corresponding failure mode is the axial tensile splitting with multiple cracks. This truly abnormal, unexpected behaviour is due to the aggregate structure, which prevents the shear band formation in this case. However, it is somewhat a "lucky strike" that this mesostructure, generated with the same parameters as those of Conc1 and Conc2, causes such a phenomenal effect. The predicted compressive/tensile strength ratio for Conc1 and Conc2 is typical ~10 but for Conc3, it is abnormal ~35. Possible additional sources for the behavior of the model with Conc3 are the 2D nature of the code and the underlying linear kinematics formulation. However, these issues are not further studied in the present paper.

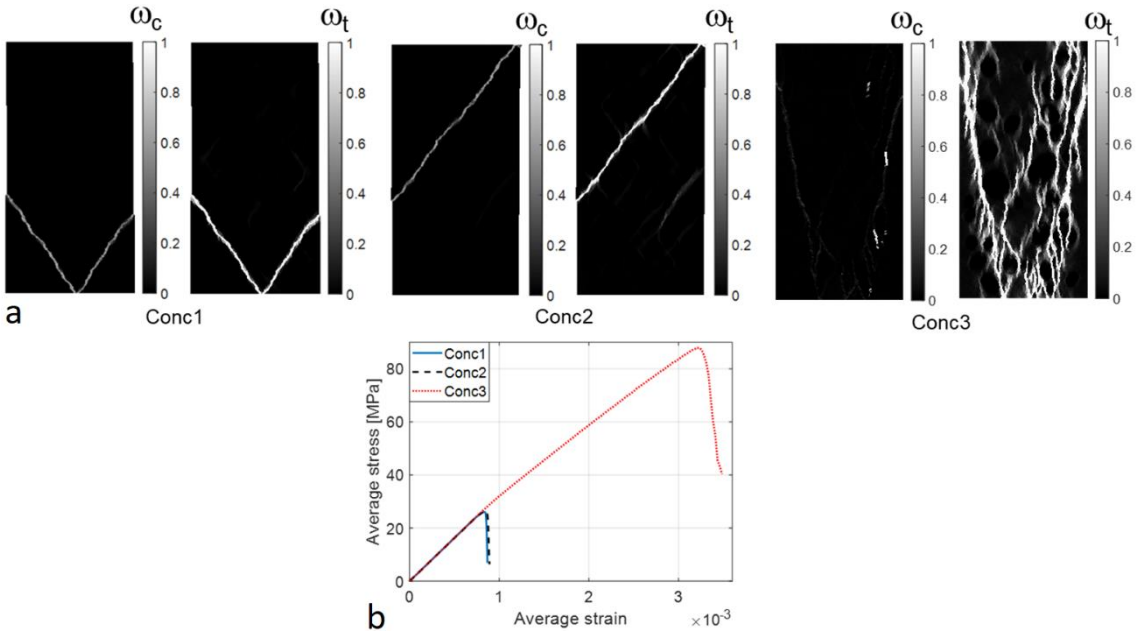

Figure 5. Simulation results for uniaxial compression test: (a) Failure modes in terms of tensile and compressive damage distributions; (b) Corresponding average stress-strain curves.

An additional concrete sample is generated to test the effect of higher aggregate-to-mortar ratio. This concrete sample, Conc4, along with the simulation results are shown in Figure 6. In uniaxial tension, the sample with much higher aggregate-to-mortar ratio exhibits response initially similar to the samples above, but a higher tensile strength reaching almost 3.3 MPa. In contrast, the post-peak behavior (Figure 6d) is substantially more ductile first since much more tensile damaging takes place, especially at ITZ areas, see Figure 6b. Then, when enough damage is developed, the stress abruptly drops to zero. In compression, a notable strengthening effect is attested, as the maximum stress reaches 87 MPa (Figure 6e). Moreover, the failure mode is the axial splitting with multiple cracks, because the dense aggregate structure prevents the shear band formation. Therefore, considering that at the lower aggregate-to-mortar ratio the transition of the failure mode from the shear banding to the axial splitting mode took place with one specimen, out of three, the (lower) ratio used above could be a threshold ratio, or close to it, beyond which this transition happens more often. However, more research is needed on this issue before more definitive conclusions can be made.

A note on the limitations of the 2D mesoscale approach is in order here. The most obvious shortcoming is that a substantially different geometries can result from a single 3D aggregate depending on the orientation and location of the 2D cut section (think about conic sections). A 2D model may thus result in different stress distributions and crack propagation patterns. Moreover, boundary conditions and interactions between the concrete phases are much more realistic in the 3D approach. The differences between the 2D and 3D modelling was compared by Zhang et al. [21] by taking a representative cut from a 3D mesoscopic model. It was found that the 2D model overestimated the compressive strength of the sample by 18 % and the post-peak part of the stress-strain response was more brittle than that in 3D. The authors speculated that the previous feature

was partly because of the underlying plane strain assumption, while the latter was attributed to more complicated crack coalescence and branching in 3D.

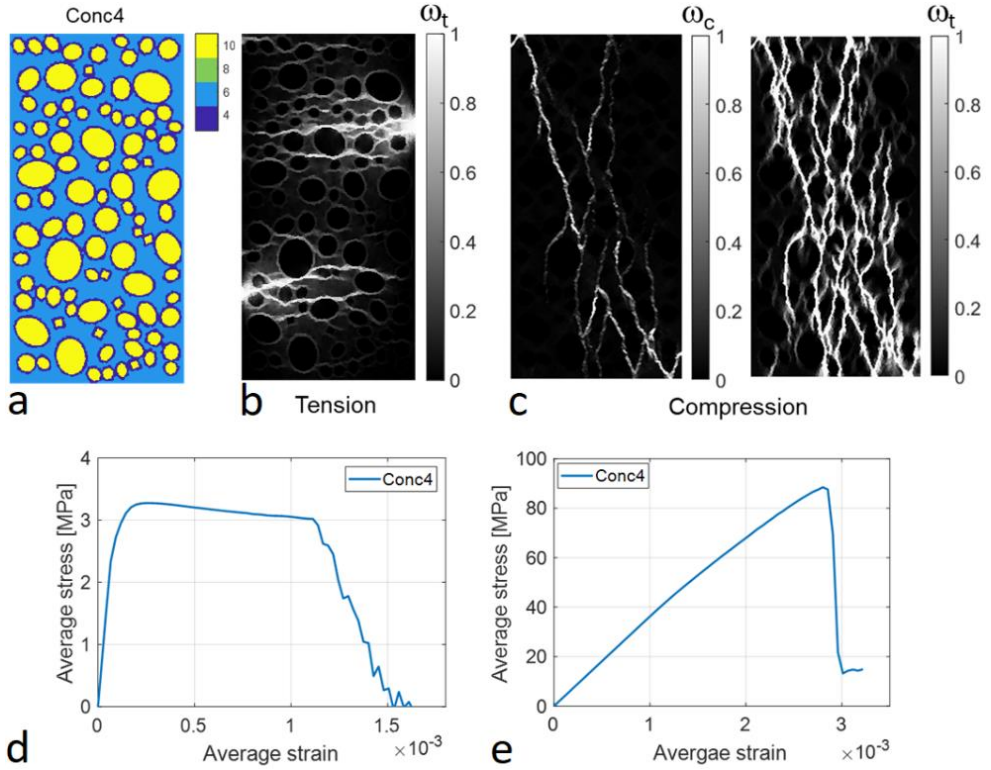

Figure 6. Simulation results for uniaxial tests (Conc4): (a) Aggregate-mortar mesostructure represented in terms of tensile strength distribution; (b) Tensile damage distribution after uniaxial tension test; (c) Tensile and compressive damage distribution after uniaxial compression test; (d) Average stress-strain curve in tension test; (e) Average stress-strain curve in compression test.

Dynamic Brazilian disc test

Brazilian disc (BD) test is a popular method to determine the tensile strength of brittle materials like rocks and concrete [22]. It is often touted that the direct tensile test is challenging to carry out adequately due to premature cracking at the grips. Hence, experimentalists tend to resort to Brazilian test, which is an indirect test based on the elasticity solution of a disc under diametral compression. However, the assumptions of Brazilian test are also challenging to fulfill because the crack initiation spot (more than) often offsets from the center and, thus, the indirect tensile strength value measured is too low [23].

The dynamic version of the test, carried out with the Split Hopkinson Pressure Bar (SHPB) device [22], in contrast to the quasi-static, tend to overestimate the indirect dynamic tensile strength calculated as

$$\sigma_t = 2P/\pi LD, \tag{15}$$

where P is the force measured in the experiment, with L and D being the length (thickness) and the diameter of the disc sample. In dynamic BD test based on the SHPB device, the disc is placed between two slender steel bars equipped with strain gages (see Figure 7). Then a striker hits the end of the incident bar and sends a compressive wave, which propagates along the bar and traverses through the sample into the transmitted bar while the sample is axially split or fragmented into debris depending on the striker velocity. This test, when based on Equation (15), usually overestimates the tensile strength because the force measured (P) increases even after the disc is split into two halves [24]. Furthermore, if the strain rate is too high, premature shear fractures occur at the contact areas resulting in imbalance of contact forces and invalid test results, because the "dynamic equilibrium" is lost. For this reason, pulse shapers are often used to smooth the stress wave. We conclude this critical discussion on Brazilian test by noting that in both the quasi-static and dynamic versions of the test, it is the narrow contact zone that is prone to premature failure of the disc material at the wrong place invalidating the results with respect to tensile strength.

Putting these critical comments aside, we now attempt to simulate the dynamic BD test on a numerical concrete disc based on the modelling principle depicted in Figure 7.

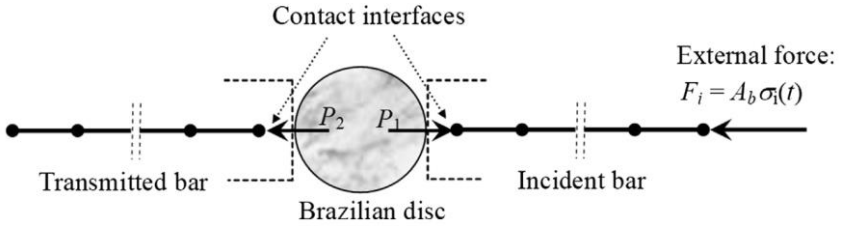

Figure 7. The modelling principle for DB test with SHPB device (A_b is the cross-sectional area of the bar).

The impact of the striker is modelled as an external force applied at the end of the incident bar, which in turn, along with the transmitted bar, is described by 2-node bar elements. Moreover, the contact constraints are imposed between the disc and the bar ends, and the contact forces P_1 and P_2 are solved, with the method described in [25]. A sinusoidal stress pulse is applied with variable amplitude and a constant length in time of 320 μs. Figure 8 shows the numerical concrete sample, the FE mesh, and simulation results for the tensile damage and the contact forces P_1 and P_2 when the amplitude of the input stress pulse is 20 MPa.

The predicted failure mode, shown in Figure 8c, is the experimental axial splitting with few cracks, notably detouring the strong aggregate located close to the center of the disc. The corresponding contact forces, both exceeding 25 kN, show reasonable "dynamic equilibrium". Thus, the indirect tensile strength given by Equation (15) is valid in this respect.

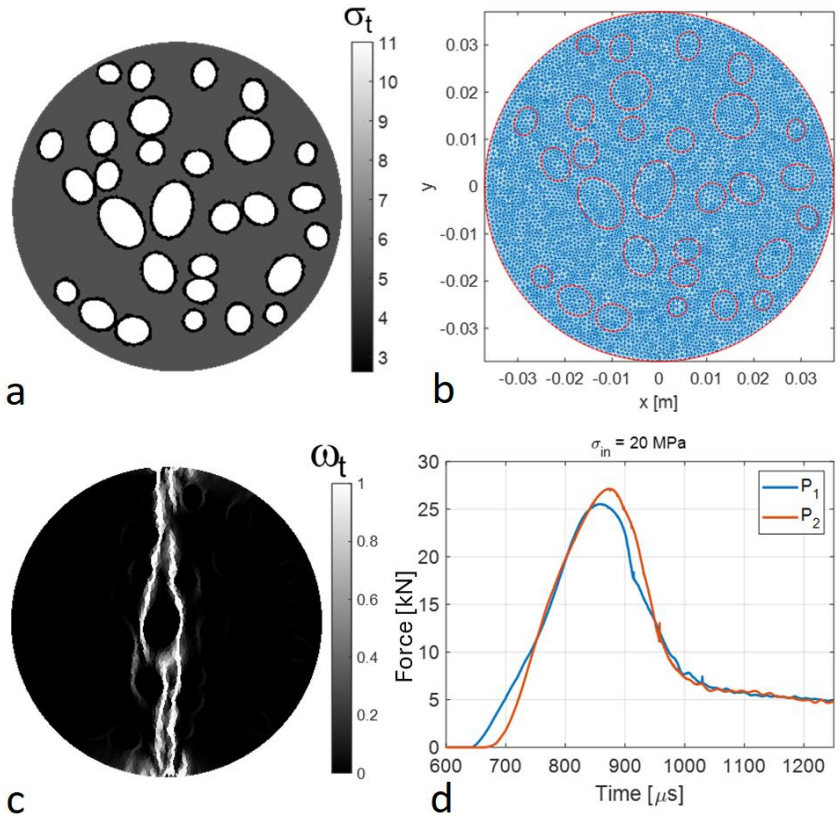

Figure 8. Simulation results for dynamic BD test (σ_{in} = 20 MPa): (a) Aggregate-mortar mesostructure of the numerical concrete disc; (b) The FE mesh with 14830 elements; (c) Tensile damage distribution at the end of simulation; (d) Contact forces as a function of time.

Moreover, the actual value, 6 MPa at the strain rate 1.24 s^{-1}, seems to be in realistic bounds when compared to the experiments on mortar reported by Yang et al. [26]. They report indirect tensile strength ranging from 4.75 MPa to 5.0 MPa at rates from 0.97 s^{-1} to 1.89 s^{-1}. The quasi-static compressive strength for this mortar is 28.7 MPa, which is reasonably close to the compressive strength, 26.3 MPa, of present numerical concrete. The quasi-static indirect tensile strength for their mortar was 4.7 MPa, which means that the dynamic increase factor (DIC) is close to 1 at strain rate ~1 s^{-1}.

Next, the incident pulse amplitude is increased to 50 MPa. The simulation results are shown in Figure 9. At a higher level of stress amplitude, resulting in strain rate $\dot{\varepsilon} = 2.6\ s^{-1}$, the amount of tensile damage has increased considerably (Figure 9a). Some radial cracking can also be observed. Moreover, the contact forces are still quite similar (see Figure 9b), so that the "dynamic equilibrium" is preserved and, thus, a tensile strength of 8.4 MPa can be read from the curve in Figure 9c. The dynamic indirect strength increases 40 % when the strain rate increases 110 %. This prediction is in realistic bounds because, e.g., Yang et al [26] report ~40 % increase in dynamic splitting (indirect tensile) strength for mortar when strain-rate increases from ~1…2 s^{-1} to ~3…4 s^{-1}. It should, however, be mentioned that the strain-rate increase effect is substantially (almost 50 %) stronger for concrete, i.e. mortar with aggregates, than for pure mortar, see Jin et al. [27]. In this respect, the present simulation results are also realistic.

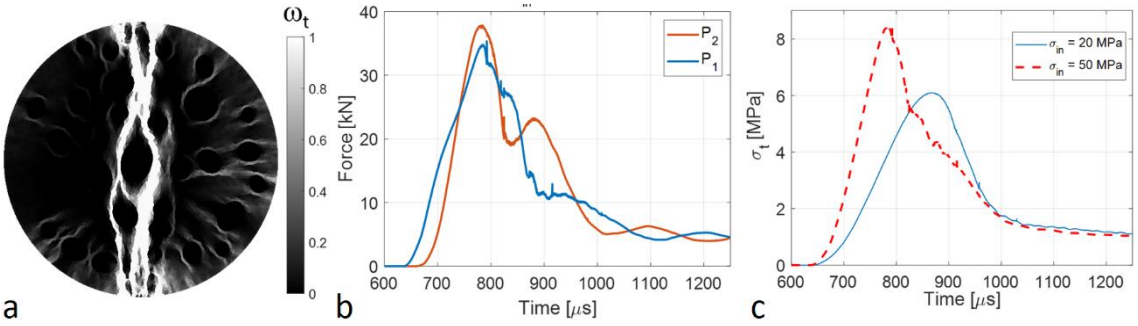

Figure 9. Simulation results for dynamic BD test (σ_{in} = 50 MPa): (a) Tensile damage distribution at the end of simulation; (b) Contact forces as a function of time; (c) Tensile stress as a function of time according to Equation (15).

Conclusions

A 2D mesomechanical method to model concrete failure under dynamic loading was developed in this paper. The Matlab-based code for concrete aggregate-mortar generation is restricted to convex polygonal aggregate shape. However, this is not a severe limitation because aggregates are mostly of this geometry. The concrete failure is described by a damage-viscoplasticity model, which cannot describe crack as a strong discontinuity but in the weak, smeared sense, as a localised deformation band. Nevertheless, the numerical simulations demonstrated that the present method predicts the salient features, i.e. the correct failure modes and the compressive-to-tensile strength ratio, under uniaxial tension and compression. Moreover, the simulations of dynamic Brazilian disc test demonstrated that the present model predicts realistic strain-rate effects for concrete. Furthermore, the numerical simulations of uniaxial tests suggest that the aggregate structure may have dramatic, unexpected effects, e.g. a threefold increase in compressive strength, on failure mode and compressive strength of concrete. However, a full 3D version of the present approach, presently under development, is needed to test whether such an anomaly is only a numerical 2D artefact. The 3D version would also solve the general shortcomings of the present 2D approach discussed above, namely the overestimation of the compressive strength and the post-peak brittleness of the stress-strain curve.

Acknowledgements

This work is funded by the Research Council of Finland via the project ConSus – Towards sustainable carbon-free concrete construction.

References

[1] J.G.M. van Mier. *Fracture processes of concrete*. Boca Raton, CRC Press, 1997. https://doi.org/10.1201/b22384

[2] H.J.G.M van Geel. Concrete behaviour in multiaxial compression: experimental research, Doctoral Dissertation, Eindhoven University of Technology, 1998. https://doi.org/10.6100/IR515170

[3] I. Vegt. Concrete in dynamic tension: The fracture process. Doctoral Dissertation, Delft University of Technology, 2016. https://doi.org/10.4233/uuid:c351e276-e7e2-4153-98e6-bea6882cfb30
[4] D. Yan, G. Lin. Dynamic properties of concrete in direct tension, *Cement and Concrete Research*, 36: 1371–1378, 2006. https://doi.org/10.1016/j.cemconcomp.2023.105150
[5] G. Hofstetter G, G. Meschke. (Eds.), *Numerical Modeling of Concrete Cracking*, CISM Courses and Lectures, vol. 532, Springer, 2011. https://doi.org/10.1007/978-3-7091-0897-0
[6] C. Zhang, K. Li, X. Hu, N. Banthia, C. Shi. A review on numerical simulation of the failure of high-performance fiber-reinforced concretes. *Journal of Sustainable Cement-Based Materials*, 13(6): 918–937, 2024. https://doi.org/10.1080/21650373.2024.2347594
[7] J. Zhang J, R. Ma, Z. Pan, H. Zhou. Review of Mesoscale Geometric Models of Concrete Materials. *Buildings*, 13(10): 2428, 2023. https://doi.org/10.3390/buildings13102428
[8] P.S.M. Thilakarathna, K.S. Kristombu Baduge, P. Mendis, V. Vimonsatit, H. Lee. Mesoscale modelling of concrete – A review of geometry generation, placing algorithms, constitutive relations and applications, *Engineering Fracture Mechanics*, 231, 106974, 2020. https://doi.org/10.1016/j.engfracmech.2020.106974
[9] T. Saksala, K. Kolari, R. Kouhia. Modelling the effect of concrete cement composition on its strength and failure behavior. *Rakenteiden Mekaniikka*, 55(3): 55–65, 2022. https://doi.org/10.23998/rm.120704
[10] P.E. Roelfstra, H. Sadouki, F.H. Wittmann, Le béton numérique. *Materials and Structures*, 18:327–335, 1985. https://doi.org/10.1007/BF02472402
[11] A-S. Dequiedt, M. Coster, J-L. Chermant, D. Jeulin, Towards a model of concrete mesostructured. *Cement and Concrete Composites*, 23(2–3):289–297, 2001. https://doi.org/10.1016/S0958-9465(00)00057-3
[12] A. Gangnant, J. Saliba, C. La Borderie, S. Morel. Modeling of the quasibrittle fracture of concrete at meso-scale: Effect of classes of aggregates on global and local behavior. *Cement and Concrete Research*, 89:35–44,2016. https://doi.org/10.1016/j.cemconres.2016.07.010
[13] R.R. Pedersen, A. Simone, L.J. Sluys. Mesoscopic modeling and simulation of the dynamic tensile behavior of concrete. *Cement and Concrete Research*, 50:74–87.2013. https://doi.org/10.1016/j.cemconres.2013.03.021
[14] T. Saksala. Numerical modelling of concrete fracture processes under dynamic loading: meso-mechanical approach based on embedded discontinuity finite elements. *Engineering Fracture Mechanics*, 201:282–297,2018. https://doi.org/10.1016/j.engfracmech.2018.07.019
[15] E.N. Landis, J.E. Bolander. Explicit representation of physical processes in concrete fracture. *Journal of Physics D: Applied Physics*, 42:214002, 2009. https://doi.org/10.1088/0022-3727/42/21/214002
[16] W.M. Wang, L.J. Sluys, R. De Borst. Viscoplasticity for instabilities due to strain softening and strain-rate softening. *International Journal for Numerical Methods*

in Engineering, 40: 3839–3864, 1997. https://doi.org/10.1002/(SICI)1097-0207(19971030)40:20<3839::AID-NME245>3.0.CO;2-6
[17] J. Lee, G.L. Fenves. Plastic-damage model for cyclic loading of concrete structures. *Journal Engineering Mechanics*, 124:892–900, 1998. https://doi.org/10.1061/(ASCE)0733-9399(1998)124:8(892)
[18] P. Grassl, M. Jirásek. Damage-Plastic model for concrete failure. *International Journal of Solids and Structures*, 43:7166–7196, 2006. https://doi.org/10.1016/j.ijsolstr.2006.06.032
[19] A. Al-Rumaithi. Aggregate 2D Packing Generator. MATLAB Central File Exchange. https://www.mathworks.com/matlabcentral/fileexchange/85503-aggregate-2d-packing-generator, Retrieved February 14, 2024.
[20] P. Wriggers, S.O. Moftah. Mesoscale models for concrete: Homogenisation and damage behaviour. *Finite Elements in Analysis and Design*, 42(7): 623–636, 2006. https://doi.org/10.1016/j.finel.2005.11.008
[21] L. Zhang, X. Sun, H. Xie, J. Feng. Three-dimensional mesoscale modeling and failure mechanism of concrete with four-phase, *Journal of Building Engineering*, 64: 105693, 2023. https://doi.org/10.1016/j.jobe.2022.105693
[22] R. Ulusay (Ed.), *The ISRM Suggested Methods for Rock Characterization, Testing and Monitoring: 2007–2014*. Springer Cham, 2014. https://doi.org/10.1007/978-3-319-07713-0
[23] C. Fairhurst. On the validity of the 'Brazilian' test for brittle materials. *International Journal of Rock Mechanics and Mining Sciences & Geomechanics Abstracts*, 1(4): 535–546, 1964. https://doi.org/10.1016/0148-9062(64)90060-9
[24] A. Wessling, J. Kajberg. Dynamic Compressive and Tensile Characterisation of Igneous Rocks Using Split-Hopkinson Pressure Bar and Digital Image Correlation. *Materials*. 15(22):8264, 2022. https://doi.org/10.3390/ma15228264
[25] T. Saksala. Damage-viscoplastic consistency model with a parabolic cap for rocks with brittle and ductile behavior under low-velocity impact loading, *International Journal for Numerical and Analytical Methods in Geomechanics*. 34:1041–1062, 2010. https://doi.org/10.1002/nag.868
[26] F. Yang, H. Ma, L. Jing, L. Zhao, Z. Wang. Dynamic compressive and splitting tensile tests on mortar using split Hopkinson pressure bar technique. *Latin American Journal of Solids and Structures*, 12(4), 730–746, 2015. https://doi.org/10.1590/1679-78251513
[27] X. Jin, C. Hou, X. Fan, C. Lu, H. Yang, X Shu, Z. Wang. Quasi-static and dynamic experimental studies on the tensile strength and failure pattern of concrete and mortar discs. *Scientific Reports*, 7: 15305, 2017. https://doi.org/10.1038/s41598-017-15700-2

Timo Saksala, Sulata Dhakal, Reijo Kouhia
Structural mechanics, BEN, Tampere University
P.O. Box 600, FI-33101 Tampere
timo.saksala@tuni.fi, sulata.dhakal@tuni.fi, reijo.kouhia@tuni.fi